

Geometric Model Predictive Path Integral for Agile UAV Control with Online Collision Avoidance

Pavel Pochobradský, Ondřej Procházka, Robert Pěnička, Vojtěch Vonásek, Martin Saska

Abstract—In this letter, we introduce Geometric Model Predictive Path Integral (GMPPPI), a sampling-based controller capable of tracking agile trajectories while avoiding obstacles. In each iteration, GMPPPI generates a large number of candidate rollout trajectories and then averages them to create a nominal control to be followed by the controlled Unmanned Aerial Vehicle (UAV). Classical Model Predictive Path Integral (MPPI) faces a trade-off between tracking precision and obstacle avoidance; high-noise random rollouts are inefficient for tracking but necessary for collision avoidance. To this end, we propose leveraging geometric SE(3) control to generate a portion of GMPPPI rollouts. To maximize their benefit, we introduce a UAV-tailored cost function balancing tracking performance with obstacle avoidance. All generated rollouts are projected onto depth images for collision avoidance, representing, to our knowledge, the first method utilizing depth data directly in a UAV MPPI loop. Simulations show GMPPPI matches the tracking error of an obstacle-blind geometric controller while exceeding the avoidance capabilities of state-of-the-art planners and learning-based controllers. Real-world experiments demonstrate flight at speeds up to 17 m/s and obstacle avoidance up to 10 m/s.

Index Terms—Collision Avoidance, Agile Flight, MPPI, Control

SUPPLEMENTARY MATERIAL

Video: <https://youtu.be/HEo4MQNX6xc>

Code: <https://github.com/ctu-mrs/gmppi>

I. INTRODUCTION

AUTONOMOUS Unmanned Aerial Vehicles (UAVs) are increasingly being deployed in missions requiring navigation in unknown cluttered environments. In various scenarios, such as search and rescue [1], power line inspection [2], and even digitization of historical monuments [3], UAVs might need to perform complex maneuvers in unknown environments while avoiding obstacles. Meanwhile, speed is an important criterion across use cases, allowing for better efficiency in the case of inspection and even helping save lives in the case of search and rescue. Control and local trajectory planning for UAVs in such conditions is a challenging open problem. Flying at higher speeds demands collision avoidance that supports rapid, agile maneuvers, but (small) UAVs are typically constrained by depth sensor range and computational capability.

The classical solution to real-time navigation in cluttered environments is modular: an environment map is built from sensor input, a global planner finds an obstacle-free trajectory,

Manuscript received: October, 9, 2025; Revised January, 13, 2026; Accepted February, 8, 2026.

This paper was recommended for publication by Editor G. Loianno upon evaluation of the Associate Editor and Reviewers' comments.

The authors are with the Multi-robot Systems Group, Faculty of Electrical Engineering, Czech Technical University in Prague, Czech Republic (<http://mrs.felk.cvut.cz/>). This work has been supported by the Czech Science Foundation (GACR) under research project No. 23-06162M, by the European Union under the project Robotics and advanced industrial production (reg. no. CZ.02.01.01/00/22_008/0004590), and by CTU grant no SGS23/177/OHK3/3T/13.

Digital Object Identifier (DOI): see top of this page.

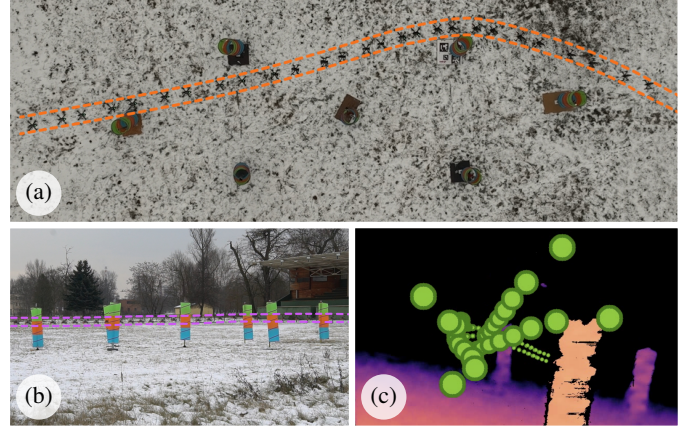


Fig. 1. Visualisation of the real-world experiment verifying the obstacle avoidance capability of the proposed controller.

and a controller executes it. In this approach, latency can accumulate, preventing flight at higher speeds [4]. Modularity often prevents the planner from considering full dynamics and the controller from accounting for obstacles, reducing agility. Moreover, a controller that is not aware of obstacles might cause a crash even if the original planned trajectory was collision-free due to, e.g., a tracking error. Recent learning-based methods aim to bypass the modular design by learning end-to-end mapping from sensor data to control commands [4], [5]. Although such methods avoid the segmentation challenges mentioned above, they require large training data and cannot be easily reused for different UAVs [6].

This letter proposes a novel UAV controller which we call Geometric Model Predictive Path Integral (GMPPPI). Based on the Model Predictive Path Integral (MPPI) method [7], GMPPPI is a sampling-based controller utilizing a Graphics Processing Unit (GPU) for parallel generation of a large number of candidate rollout trajectories in each iteration, resulting in obstacle avoidance and agile UAV control capability. Like learning-based methods [4], [5], our approach unifies planning and control, but requires no training and is reusable across UAVs by modifying parameters. Tuning existing MPPI methods [7] requires balancing trajectory tracking precision, flight smoothness, and obstacle avoidance capability. In particular, rollout trajectories generated by adding noise to a nominal trajectory do not represent an efficient way of following a reference trajectory.

Therefore, in addition to random rollouts, we propose using geometric SE(3) control [8] to generate a portion of the GMPPPI rollout trajectories, enabling precise reference tracking. Notably, even a small number of such SE(3)-based rollouts significantly improves trajectory tracking performance compared to prior MPPI approaches [7]. To maximize this benefit, we introduce a UAV-tailored GMPPPI cost function, which enables us to retain the tracking capability of SE(3)

control alongside the obstacle avoidance capability. Furthermore, to the best of our knowledge, we introduce the first method utilizing depth sensor data directly in a UAV MPPI-based controller loop. We also adopt a variable time-step sampling strategy, balancing the importance of near and distant trajectory segments while fully exploiting sensor range. Simultaneously, deterministic yaw control improves sampling performance without increasing the number of samples.

We show that in trajectory tracking tasks, the proposed GMPPI controller achieves a tracking error similar to geometric SE(3) control [8] and significantly smaller than an existing MPPI controller [7]. Through an ablation study, we highlight the contribution of each of the GMPPI features to overall performance, namely integration of SE(3) rollouts, variation of noise and cost parameters with time step and dynamic rollout time step length. In obstacle avoidance capability, GMPPI exceeded the performance of the learning-based controllers [4], [5] and of the state-of-the-art obstacle-aware Bubble planner [9]. In real-world deployment, shown in Fig. 1, the proposed controller is capable of avoiding obstacles at speeds of up to 10 m s^{-1} .

II. RELATED WORK

1) *Trajectory Tracking*: Quadrotor trajectory tracking ranges from linear Proportional Integral Derivative (PID) to Nonlinear Model Predictive Control (NMPC) [10] and SE(3) control [8]. SE(3) control stands out due to its almost global exponential stability [8], enabling aggressive flight at the limit of dynamics as long as the reference trajectory is feasible. Its low computational overhead allows fast on-board processing and integration into the proposed controller, while its tracking capability makes it a suitable benchmark.

2) *Obstacle Avoidance*: The task of UAVs avoiding obstacles is generally handled as part of local trajectory optimization either by a local planner [9] or a controller [11]. One of the oldest methods of real-time replanning and optimization of collision-free trajectories utilized Artificial Potential Field (APF) [12], where an artificial force defined as the gradient of an APF acts on the trajectory, the goal position has the lowest potential, and states with a possible collision have a high potential. Alternatively, Vector Field Histogram (VFH) [13] and VFH+ [14] discretize the possible trajectories into a polar histogram and balance path smoothness, distance to goal, and obstacle avoidance. Both APF and VFH+ have been applied to UAV obstacle avoidance in [15] and [16], respectively.

APF and VFH+ cannot take full advantage of the agility of some UAVs. Directly finding a safe, e.g., time-optimal trajectory utilizing the full UAV agility while avoiding obstacles is not computationally feasible in real time. Instead of directly optimizing the trajectory, precomputed motion primitives can be used to build a feasible trajectory. Such primitives can be state-based, control-based, or motion-based [17]. Improvements to motion primitive-based search algorithms for local obstacle-aware trajectory planning were developed in [18]. To further decrease trajectory computation time and latency, the mapping step can be bypassed.

Methods such as [17] or [19] use most recent image data to generate local trajectories. Despite integration of these

methods into navigational pipelines and extensive testing [20], they cannot utilize the full dynamic capabilities of agile UAVs.

As the quadrotor UAV is differentially flat [21], an alternative to motion primitive-based planning is to directly solve the trajectory optimization problem by creating polynomial trajectories [22]. The method [22] has been applied along with a corridor planner in [9], with performance exceeding some methods based on Imitation Learning (IL) [4]. Alternatively, obstacle avoidance can be included as a condition of trajectory optimization [11] in an adapted Model Predictive Control (MPC) controller, though this is computationally demanding.

Although recent methods utilizing separate mapping, planning and control modules have significantly advanced agile flight capabilities [9], alternatives mitigating latency have been explored, such as learning-based approaches that generate control commands from sensor inputs [4], using either Reinforcement Learning (RL) [23] or IL [4]. Although these methods produce impressive results, they embed very little prior information about the systems they are controlling, treating them instead as black boxes. The controller must therefore be retrained after any change to the parameters of the controlled UAV, such as mass. Additionally, RL and IL methods have very low sample efficiency [24]. Recent research has suggested mitigating the low sample efficiency by using differentiable simulations [5], but it does not mitigate the other drawbacks of learning-based methods.

3) *Model Predictive Path Integral*: MPPI is a variant of MPC utilizing principles of Path Integral [25] control. While traditional MPC solves local trajectory optimization using iterative methods, MPPI uses a Monte Carlo sampling-based approach [26], allowing it to work with gradient-free and non-smooth cost functions.

Pure MPPI control has a number of drawbacks. First, a good initialization of the nominal commands is required. For UAV control, this can be solved by reusing the results of previous MPPI iterations. Second, disturbances that are not taken into account by the model used for path integration can cause issues with convergence. This can be addressed by generating rollouts from the desired state and implementing an ancillary controller to follow this trajectory, effectively using the MPPI only as a local planner and delegating the controller functionality [27].

MPPI has been explored for quadrotor control in both simulation [28] and real-world experiments [7]. Although a potential for trajectory tracking and obstacle avoidance has been demonstrated, obstacle avoidance was limited to hard-coded obstacles. Moreover, no configuration of MPPI demonstrated the ability to combine effective obstacle avoidance with agile and smooth trajectory tracking at the level achieved by methods dedicated to each task individually.

More recently, Perception-Aware MPPI (PA-MPPI) [29] was introduced, which augments MPPI with perception objectives for exploration when the goal is occluded. This extends MPPI toward global navigation, while our approach focuses on local planning and control for agile flight with collision avoidance.

III. METHODOLOGY

This section begins with a brief overview of MPPI control. Then it details the architecture of the proposed GMPPI

controller, highlighting the integration of depth sensing, implementation of rollouts generated using an SE(3) controller, and the development of a custom cost function enabling agile and smooth flight as well as obstacle avoidance.

The base MPPI terminology and notation shown in this section are adopted from [7], where the complete method is presented. MPPI, when used as a controller, is capable of tracking trajectories while avoiding obstacles. It is first initialized with a nominal control sequence $\mathbf{u}^{\text{nom}} = [\mathbf{u}_0^{\text{nom}}, \dots, \mathbf{u}_{N-1}^{\text{nom}}]$, where the lower index j , $0 \leq j < N$, indicates a value at the j th time step of a sequence (i.e., $u_j \in \mathbf{u}^{\text{nom}}$). In each iteration, K disturbance sequences $\delta \mathbf{u}_j^k$, each of length N , are sampled from a normal distribution with zero mean. Rollout commands \mathbf{u}_j^k and states \mathbf{x}_{j+1}^k are then computed as

$$\left. \begin{aligned} \delta \mathbf{u}_j^k &\in \mathcal{N}(0, \Sigma), \\ \mathbf{u}_j^k &= \mathbf{u}_j^{\text{nom}} + \delta \mathbf{u}_j^k, \\ \mathbf{x}_{j+1}^k &= \mathbf{x}_j^k + \mathbf{f}_{\text{RK4}}(\mathbf{x}_j^k, \mathbf{u}_j^k, \Delta t), \end{aligned} \right\} \begin{aligned} k &= 1, \dots, K, \\ j &= 0, \dots, N-1. \end{aligned} \quad (1)$$

For UAV control, the state is $\mathbf{x} = [\mathbf{p}^T \ \mathbf{v}^T \ \mathbf{q}^T \ \boldsymbol{\omega}^T]^T$, consisting of the position, velocity, and body rate vectors $\mathbf{p}, \mathbf{v}, \boldsymbol{\omega} \in \mathbb{R}^3$, respectively, and unit quaternion rotation on the rotation group $\mathbf{q} \in \mathbb{S}\mathbb{O}(3)$. Commands $\mathbf{u} = [F_t \ \boldsymbol{\omega}_c]$ consist of the total desired thrust $F_t \in \mathbb{R}^+$ and angular velocity $\boldsymbol{\omega}_c \in \mathbb{R}^3$. Commands are limited to $F_{t,\min} \leq F_t \leq F_{t,\max}$, $|\omega_{c,x}| \leq \omega_{xy,\max}$, $|\omega_{c,y}| \leq \omega_{xy,\max}$ and $|\omega_{c,z}| \leq \omega_{z,\max}$ before being used to generate a rollout trajectory. The values of the time step Δt used in GMPPI are described in Sec. III-B. Dynamics of the UAV are defined by

$$\begin{aligned} \dot{\mathbf{p}} &= \mathbf{v}, \quad \dot{\mathbf{q}} = \frac{1}{2} \mathbf{q} \odot \begin{bmatrix} 0 \\ \boldsymbol{\omega} \end{bmatrix}, \quad \dot{\boldsymbol{\omega}} = \mathbf{J}^{-1} (\boldsymbol{\tau} - \boldsymbol{\omega}_c \times \mathbf{J} \boldsymbol{\omega}_c), \\ \dot{\mathbf{v}} &= \frac{1}{m} \mathbf{R}(\mathbf{q}) \left([0 \ 0 \ F_t]^T - \mathbf{D} \mathbf{R}(\mathbf{q})^T \mathbf{v} \right) + \mathbf{g}, \end{aligned} \quad (2)$$

with Runge-Kutta 4 being used in (1) for forward integration. $\mathbf{R}(\mathbf{q})$ is a rotation matrix corresponding to the quaternion \mathbf{q} and air resistance of the UAV is approximated by a linear drag with coefficients $\mathbf{D} = \text{diag}(c_x, c_y, c_z)$.

Each rollout state sequence \mathbf{x}^k is evaluated by a cost function to produce a cost C^k . Trajectories colliding with an obstacle and trajectories further from the reference receive higher costs. The proposed GMPPI cost function mapping rollout state sequences \mathbf{x}^k to costs C^k is presented in Sec. III-E. Costs C^k are used to compute rollout weights w_k using

$$\begin{aligned} \rho &= \min\{C^1, \dots, C^K\}, \quad \tau_k = -\frac{1}{\lambda} (C^k - \rho), \\ \eta &= \sum_{k=1}^K \exp(\tau_k), \quad w_k = \frac{1}{\eta} \exp(\tau_k), \end{aligned} \quad (3)$$

with the parameter λ controlling the degree to which a difference in cost between two trajectories causes a difference in their final weights. Finally, the nominal control actions are set to the weighted average of the rollout commands

$$\mathbf{u}_j^{\text{nom}} := \sum_{k=1}^K w_k \cdot \mathbf{u}_j^k \quad (4)$$

and the first command $\mathbf{u}_0^{\text{nom}}$ is applied to the controlled UAV.

A. Depth Camera Integration

To the best of our knowledge, no MPPI implementation has yet been integrated with a depth sensor for agile collision avoidance. To minimize delay, we avoid map construction or heavy model processing [4]. Instead, we use the available rollout states $\mathbf{x}_j^k = [\mathbf{p}_j^{kT} \ \mathbf{v}_j^{kT} \ \mathbf{q}_j^{kT} \ \boldsymbol{\omega}_j^{kT}]^T$.

The length L , width W and height H of the UAV are used to define a set

$$\mathcal{H}_j^k = \left\{ \mathbf{p}_j^k + \frac{\epsilon}{2} \begin{bmatrix} \sigma_1 L \\ \sigma_2 W \\ \sigma_3 H \end{bmatrix} \middle| \sigma_1, \sigma_2, \sigma_3 \in \{-1, 1\} \right\} \quad (5)$$

of all corner points of the UAV shifted outwards by a safety multiplier $\epsilon > 1$. We project each of the corner points as well as the UAV center point $\mathbf{p}_{\text{proj}} \in (\mathcal{H}_j^k \cup \{\mathbf{p}_j^k\})$ onto the latest available depth image to determine if a collision occurs (see Fig. 2). This approach eliminates nearly all sources of latency, with the exception of that introduced by the camera frame rate.

The sensor used in this work is a depth camera with an intrinsic matrix \mathbf{K} that describes the transformation from the camera reference frame C to the image reference frame I . The camera is rigidly mounted to the UAV, with the transformation from the body-fixed frame B to C described by a matrix \mathbf{M} . The transformation from B to the world frame W at the time of the latest image being captured is described by $\mathbf{R}(\mathbf{q})_l$.

The position of each projected point \mathbf{p}_{proj} in the camera reference frame C is obtained as

$${}^C \mathbf{p}_{\text{proj}} = (\mathbf{R}(\mathbf{q})_l \mathbf{M})^{-1} \mathbf{p}_{\text{proj}}. \quad (6)$$

This approach allows reusing a single image across multiple control iterations as it automatically compensates for the position and orientation shift of the UAV since the last image was taken. The distance of the rollout state position from the camera $\|{}^C \mathbf{p}_{\text{proj}}\|$ is compared to the distance d_{px} measured by the camera at the pixel coordinates ${}^I \mathbf{p}_{\text{proj}} = \mathbf{K}^C \mathbf{p}_{\text{proj}}$, where the rollout position is projected on the depth image.

The existence of a collision is determined using

$$\text{Col}(\mathbf{p}_{\text{proj}}) = \mathbb{1} \left\| \|{}^C \mathbf{p}_{\text{proj}}\| \in [d_{px}, d_{px} + d_a] \right\} \quad (7)$$

is defined, which returns 1 if the distance of the relevant trajectory point \mathbf{p}_{proj} from the camera is similar to the distance d_{px} measured by the camera at the pixel where \mathbf{p}_{proj} would appear on the depth image. Instead of assuming all space behind an obstacle is occupied, a depth d_a is assumed to allow the controller to optimistically plan a return path to the reference trajectory even if the path is not fully visible yet. If a projection falls outside of the visible area, the nearest pixel of the depth image is used to estimate the presence of obstacles that are partially outside of the field of view of the camera.

B. Dynamic Rollout Time Steps

Small UAVs are limited in terms of the on-board hardware, which in turn limits the computational power. This restricts the number of rollouts and the number of steps in each rollout.

To ensure that the sensor range, labelled s , is fully utilized at any flight speed, a vector $\mathbf{n} = [n_0, \dots, n_{N-1}]$ is defined,

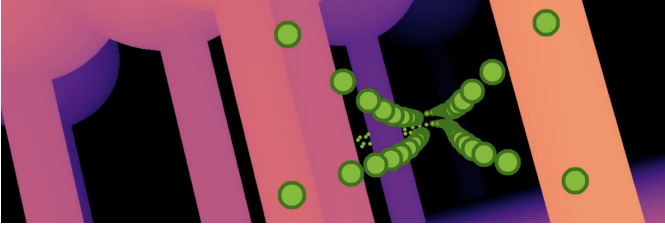


Fig. 2. Depth-camera image with the projection of the front four corners of the UAV collision box as defined in (5) in each of the positions in the nominal trajectory $\mathbf{p}_j^{\text{nom}} \forall j \in (0, N+1)$, which is the result of applying the nominal control sequence $\mathbf{u}_j^{\text{nom}} \forall j \in (0, N)$ to the UAV in its current state.

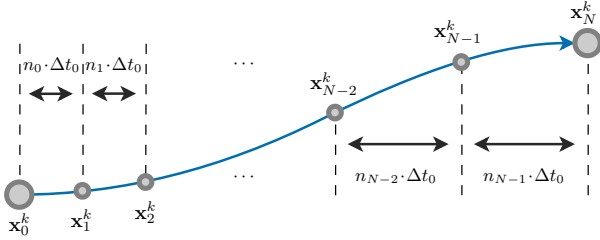


Fig. 3. Illustration of the layout of the rollout states \mathbf{x}_j^k in time. Earlier steps are shorter to ensure precision, while later steps are longer and their length is dynamically adjusted to use the full range of the available depth sensor.

where each element n_j acts as a time step multiplier at the j th step of each rollout. The corresponding time step is calculated as $\Delta t_j = n_j \Delta t_0$, where $\Delta t_0 = 0.01\text{s}$ is the base controller update period.

The first M multipliers are fixed at smaller values represented by n_{near} to maintain good simulation precision near the current state. The remaining $N - M$ multipliers are set based on the average speed of the UAV across the nominal state sequence $v_{\text{avg}}^{\text{nom}}$ and the sensor range s such that

$$n_{\text{far}} = \frac{\frac{s}{v_{\text{avg}}^{\text{nom}} \Delta t_0} - \sum_{j=0}^M n_j}{N - M}, \quad (8)$$

which ensures that the range s of the used sensor is fully utilized. The vector \mathbf{n} has values

$$n_{0 \dots M-1} = n_{\text{near}}, \quad n_{M \dots N-1} = n_{\text{far}} \quad (9)$$

and the layout of a typical rollout is illustrated by Fig. 3.

Aside from the sensor usage benefits, shorter time steps at the beginning of the rollout increase the importance of near-term flight precision and thus stability of GMPPI in hover.

C. Deterministic Yaw Control

A key factor influencing performance of MPPI-based control is the density of the simulated rollout trajectories in the space of all possible rollout trajectories. To increase this density without adding more rollouts, a dimension can be removed from the space.

This can be achieved by modifying the existing sampling-based MPPI [7] rollout generation method to control the yaw axis rotation deterministically. A proportional controller has been chosen for simplicity. It follows the reference heading \mathbf{h}^{ref} by computing

$$\boldsymbol{\omega}_z = k_{\text{MPPI},z} \angle(\mathbf{h}, \mathbf{h}^{\text{ref}}) + \boldsymbol{\omega}_{z,\text{ref}}, \quad (10)$$

where $k_{\text{MPPI},z}$ is the proportional feedback gain and $\angle(\cdot, \cdot)$ denotes the angle between two vectors.

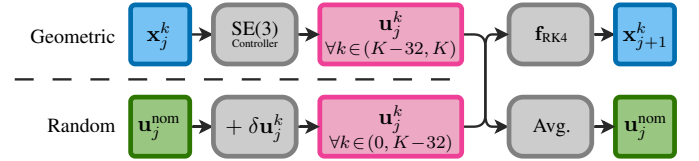


Fig. 4. Combination of geometric and random rollouts. A total of K rollout sequences are simulated, of which $K - 32$ are random and 32 use geometric control. All rollout commands are used to compute the next nominal command sequence $\mathbf{u}_j^{\text{nom}}$ as well as the next set of rollout states \mathbf{x}_{j+1}^k .

D. Geometric Control in Candidate MPPI Trajectories

In MPPI, the rollout command sequences \mathbf{u}_j^k are generated by adding random noise $\delta \mathbf{u}_j^k$ to the nominal command sequence $\mathbf{u}_j^{\text{nom}}$. Such rollouts explore the space for a collision-free trajectory, but are not efficient at precisely following reference trajectories. This motivates the search for rollout methods, which would allow precise trajectory tracking. One such option is a geometric SE(3) controller.

The geometric SE(3) controller [8] is a theoretically proven and practically validated method capable of following reference trajectories precisely and in a computationally efficient manner. One of the practical downsides of this method is the tuning process. It requires precise selection of gains, which often need to vary not just based on the controlled UAV, but also the specific trajectory to be followed.

MPPI and SE(3) control methods have complementary strengths and weaknesses. Using the SE(3) controller as a rollout generation method produces rollouts capable of tracking a reference trajectory while the generation remains computationally feasible. The remaining sampling-based rollouts can then focus on obstacle avoidance and exploration, as they no longer need to be used for following the reference trajectory.

Moreover, because MPPI already runs hundreds of parallel rollouts, more than a single SE(3) rollout may be added. The amount of rollouts generated using SE(3) is labelled K_{SE3} , with the other $K - K_{\text{SE3}}$ remaining as before. In practice, rollouts run on a GPU in warps of 32, so $K_{\text{SE3}} = 32$ is chosen, with the split between random and geometric rollouts illustrated in Fig. 4. Each of the SE(3) rollouts uses different parameters and multiple SE(3) configurations are therefore tested simultaneously, with the best configuration being selected by the proposed GMPPI cost function. Little benefit would arise from increasing or tuning the K_{SE3} parameter, as the majority of the rollouts must remain sampling-based to preserve the ability to avoid obstacles. The resulting controller can precisely track reference trajectories and avoid small unmapped obstacles.

To use a different geometric controller configuration in each rollout, the noise $\delta \mathbf{k}_{\text{SE3}}^k \in \mathcal{N}(0, \Sigma_{\text{SE3}})$ is sampled from a normal distribution with zero mean and a covariance matrix Σ_{SE3} . This noise is then added to a vector of GMPPI parameters specifying a base geometric controller configuration $\mathbf{k}_{\text{SE3}} = [k_{p_{xy}} \ k_{p_z} \ k_{v_{xy}} \ k_{v_z} \ k_{r_{xy}} \ k_{r_z}]$ creating a new configuration specific to the rollout at index k and defined by the parameters

$$\mathbf{k}_{\text{SE3}}^k = \mathbf{k}_{\text{SE3}} + \delta \mathbf{k}_{\text{SE3}}^k. \quad (11)$$

The values of the vector $\mathbf{k}_{\text{SE3}}^k$ are then used as parameters of the SE(3) controller [8].

E. Cost Function

MPPI computes a nominal trajectory as a weighted average of rollout trajectories (where higher weights w_k are assigned to rollout trajectories with a better, i.e. lower cost, behaviour (3)). Lower cost C^k is assigned to trajectories conforming the objective of the control, while higher costs are assigned to trajectories that exhibit unwanted characteristics such as excessive maneuvers or a large tracking error. The proposed controller has three goals, which are precise trajectory tracking, smooth flight, and obstacle avoidance, which always takes precedence. In GMPPI, the cost function selects whether the geometric or sampling-based rollouts should be prioritized.

Each unwanted characteristic is penalized by one or more cost components, where a measure of the unwanted characteristic is multiplied by a cost coefficient. These coefficients are parameters of GMPPI and they are dependent on the time index j in the rollout, which allows prioritizing precise trajectory tracking and smooth flight early in the rollout and exploration later in the rollout.

1) *Tracking Precision* : To enable precise trajectory tracking, the errors in position, velocity, orientation, and angular velocity relative to their reference values are computed as

$$\begin{aligned} e_p &= \|\mathbf{p}_j^k - \mathbf{p}_j^{\text{ref}}\|_2, & e_v &= \|\mathbf{v}_j^k - \mathbf{v}_j^{\text{ref}}\|_2, \\ e_q &= d_{\mathbf{q}}(\mathbf{q}_j^k, \mathbf{q}_j^{\text{ref}}), & e_\omega &= \|\boldsymbol{\omega}_j^k - \boldsymbol{\omega}_j^{\text{ref}}\|_2, \end{aligned} \quad (12)$$

where $d_{\mathbf{q}}(\mathbf{q}_1, \mathbf{q}_2)$ is an approximation of orientation difference adopted from [7] and defined as

$$d_{\mathbf{q}}(\mathbf{q}_1, \mathbf{q}_2) = 1 - \langle \mathbf{q}_1, \mathbf{q}_2 \rangle^2. \quad (13)$$

The errors are multiplied by the position c_j^p , velocity c_j^v , orientation c_j^q and angular velocity c_j^ω coefficients respectively. The coefficients can vary with the time index j in the rollout. This allows assigning a lower cost to those rollout trajectories that deviate from the reference trajectory only in later steps of the rollout simulation, which promotes exploration and reallocates precision emphasis toward earlier timesteps of the simulated rollout trajectories, allowing the controller to maximize the use of the precision of the SE(3) rollouts. This increases trajectory tracking precision, as well as smoothness. Using the Euclidean norm for position instead of its square requires computing a square root but prevents the creation of an erratic nominal trajectory in cases where a larger deviation from the reference trajectory is necessary to avoid an obstacle.

2) *Smoothness* : To promote smooth flight, two cost components are added. First, cost is added for jerk $\|\dot{\mathbf{a}}\|$, which is larger than a multiple t_j of the jerk present in the reference trajectory $\|\dot{\mathbf{a}}^{\text{ref}}\|$. The excess jerk quantity

$$e_j = \max\left(\|\dot{\mathbf{a}}_j^k\| - t_j \|\dot{\mathbf{a}}^{\text{ref}}\|, 0\right) \quad (14)$$

is introduced and multiplied by a coefficient c_j^j . This punishes any excess control input based on how much it disturbs the smoothness of the flight, while still allowing sharp trajectories to be followed precisely. This is a key feature allowing the controller to use the full potential of agile SE(3)-generated rollout trajectories if the reference trajectory contains sharp maneuvers. The reference and rollout jerk values are calculated using a finite-difference approximation from acceleration

data. Noise amplification concerns do not apply, as both the reference and rollout trajectories are noise-free.

Second, a cost is added for any difference in position

$$e_s = \|\mathbf{p}_j^k - \mathbf{p}^{\text{nom}}\| \quad (15)$$

between the rollout and the nominal trajectory. This is multiplied by a coefficient c_j^s and prevents the trajectory and therefore the control input from changing excessively between successive controller runs.

3) *Obstacle Avoidance* : Obstacle avoidance capability is introduced by assigning cost to any rollout that collides with an obstacle. The set of points $\mathcal{H}_j^k \cup \{\mathbf{p}_j^k\}$, defined in Sec. III-A, is a collision box for the UAV and the function $Col(\mathbf{p}_{\text{proj}})$, defined in (7), returns 1 when a collision is detected. When a collision occurs at step j of a rollout trajectory, the cost is scaled by $(N - j)$ so that collisions occurring earlier in the rollout are penalized more heavily than those further in the future. The obstacle cost is therefore defined as

$$e_{\text{obs}} = (N - j) \sum_{\mathbf{p}_{\text{proj}} \in (\mathcal{H}_j^k \cup \{\mathbf{p}_j^k\})} Col(\mathbf{p}_{\text{proj}}), \quad (16)$$

and is further weighted by a coefficient c_j^{obs} . This formulation provides a graded penalty rather than a binary collision/no-collision outcome, which allows for a more informed selection of candidate trajectories.

4) *Resulting Cost Function* : The combined cost for a single point in a single rollout is defined as

$$\begin{aligned} \mathbf{c}_j &= [c_j^p \quad c_j^v \quad c_j^q \quad c_j^\omega \quad c_j^j \quad c_j^s \quad c_j^{\text{obs}}], \\ \mathbf{e}_j^k &= [e_p \quad e_v \quad e_q \quad e_\omega \quad e_j \quad e_s \quad e_{\text{obs}}]^T, \\ C_j^k &= \mathbf{c}_j \cdot \mathbf{e}_j^k, \end{aligned} \quad (17)$$

resulting in the overall cost of a single rollout k to be

$$C^k = \sum_{j=1}^N C_j^k. \quad (18)$$

The entire GMPPI algorithm is summarized in Alg. 1. On lines 1–3, nominal and reference commands are resampled using the dynamic timesteps. The algorithm then creates K rollouts in parallel. On lines 4–11, K_{SE3} geometric rollouts are created by selecting the SE(3) parameters to use and then running the simulation. On lines 12–16, random rollouts with proportional yaw control are calculated. All rollouts are assigned a cost on lines 17–18, and finally, the new nominal command is created as a weighted average of rollouts on line 19. The first nominal command is used by the UAV.

IV. RESULTS

This section presents the results of conducted experiments. First, simulations verifying the ability to track agile trajectories were conducted, including an ablation study showing the benefit of each feature described in Sec. III. Next, obstacle avoidance capability has been shown in simulation and compared against three existing methods. Finally, the results of real-world experiments are presented.

All simulated experiments were conducted on a laptop with an Intel Core i7-1165G7 CPU and an NVIDIA GeForce MX450 GPU, which the proposed controller utilizes for parallel rollout simulation. Real-world experiments utilized

Algorithm 1: Single iteration of Geometric MPPI

Input: Current state estimation $\hat{\mathbf{x}}$, Nominal command sequence $\mathbf{u}_{\text{in}}^{\text{nom}}$, Reference command sequence $\mathbf{u}_{\text{in}}^{\text{ref}}$, Depth Image

Params: Number of rollouts K , Number of geometric rollouts K_{SE3} , Rollout length N , Rollout noise Σ , SE3 Parameter noise Σ_{SE3}

```

1  $\Delta t = \text{ComputeTimesteps}()$ 
2  $\mathbf{u}^{\text{nom}} = \text{ResampleNominalCommands}(\mathbf{u}_{\text{in}}^{\text{nom}}, \mathbf{n})$ 
3  $\mathbf{u}^{\text{ref}} = \text{ResampleReferenceCommands}(\mathbf{u}_{\text{in}}^{\text{ref}}, \mathbf{n})$ 
// Simulate  $K$  rollouts (Parallel on GPU)
4 for  $k = 1, \dots, K$  do
5    $\mathbf{x}_0^k = \hat{\mathbf{x}}$ 
6   if  $k < K_{\text{SE3}}$  then // SE(3) Rollout
7      $\delta \mathbf{k}_{\text{SE3}}^k \sim \mathcal{N}(0, \Sigma_{\text{SE3}})$ 
8      $\mathbf{k}_{\text{SE3}}^k = \mathbf{k}_{\text{SE3}} + \delta \mathbf{k}_{\text{SE3}}^k$ 
9     for  $j = 0, \dots, N$  do
10       $\mathbf{u}_j^k = \text{SE3Command}(\mathbf{x}_j^k, \mathbf{k}_{\text{SE3}}^k)$ 
11       $\mathbf{x}_{j+1}^k = \mathbf{x}_j^k + \mathbf{f}_{\text{RK4}}(\mathbf{x}_j^k, \mathbf{u}_j^k, \Delta t_j)$ 
12   else // Random Rollout
13     for  $j = 0, \dots, N$  do
14        $\delta \mathbf{u}_j^k \sim \mathcal{N}(0, \Sigma)$ 
15        $\mathbf{u}_j^k = \mathbf{u}^{\text{nom}} + \delta \mathbf{u}_j^k$ 
16        $\omega_z = k_{\text{MPPI},z} \angle(\mathbf{h}, \mathbf{h}^{\text{ref}}) + \omega_{z,\text{ref}}$ 
17        $\mathbf{x}_{j+1}^k = \mathbf{x}_j^k + \mathbf{f}_{\text{RK4}}(\mathbf{x}_j^k, \mathbf{u}_j^k, \omega_z, \Delta t_j)$ 
18    $C_j^k = \text{CalculateCost}(c_j^k, \mathbf{x}_{j+1}^k, \mathbf{x}_{j+1}^{\text{ref}}, \text{Depth Image})$ 
19    $C^k = \sum_{j=0}^N C_j^k$ 
20  $\mathbf{u}_0^{\text{nom}} = \text{AverageWeighedCommands}()$  // Eq. (4)

```

a Jetson Orin NX high-level computing unit with an 8-core Arm Cortex-A78AE CPU and an Ampere GPU with GMPPI controller outputs fed into a PX4 low-level flight controller. An Intel RealSense D435i depth camera set to a resolution of 640x480 px was used. All reference trajectories were generated either by an MPC-based tracker [30] or by a polynomial trajectory planner [31].

A. UAV & Controller Parameters

The UAV mass m , the arm length l , the inertia matrix \mathbf{J} and the rotor torque constant c_{tf} of the simulated UAV are shown in Table I. The parameters of the UAV used for real-world experiments were similar. The GMPPI parameters along with control input limits for both the minimum and maximum thrust $F_{t,\text{min}}, F_{t,\text{max}}$ as well as the maximum absolute angular rate ω_{max} are shown in Table II.

For obstacle avoidance in simulation, a stereo depth camera with a range of $s = 13$ m is mounted to the UAV, although the rollout length is limited to 10 m. The controller treats every visible obstacle as occupying $d_a = 2.0$ m along the viewing ray before free space is presumed. All experiments had the

TABLE I
UAV PARAMETERS USED FOR ALL SIMULATED RUNS

Model Parameters	Dimensions	Drag Coefficients
m [kg]	1.21	L [m] 0.35 c_x 0.28
l [m]	0.15	W [m] 0.35 c_y 0.35
c_{tf} [m]	0.012	H [m] 0.215 c_z 0.7
Inertia Matrix	\mathbf{J} [gm ²]	diag([7.06 7.06 13.6])

TABLE II
CONTROLLER PARAMETERS AND LIMITS

MPPI Parameters	SE3 Parameters	Control Limits
K	768	k_p [6.0 6.0 15.0] $F_{t,\text{min}}$ [N] 0.46
K_{SE3}	32	k_v [4.0 4.0 8.0] $F_{t,\text{max}}$ [N] 20.6
N	30	k_r 5.0 $\omega_{xy,\text{max}}$ [rads ⁻¹] 10.0
$k_{\text{MPPI},z}$	2.0	$\omega_{z,\text{max}}$ [rads ⁻¹] 2.0

TABLE III
RELATIONSHIP OF SPEED AND CAMERA TILT

Speed [m s ⁻¹]	3	5	7	9	10	11	12	13
Tilt [deg]	8	10	16	22	22	27	27	30

camera tilted up by a fixed angle to allow full use of the sensor range. Parameters are shown in Table III.

The relative size of cost parameters from (17), shown in Fig. 5a, c_j^p , c_j^v , c_j^a and c_j^ω is based on an existing MPPI implementation [7]. They are, however, also dependent on the rollout index j . c_j^p , c_j^a and c_j^ω decrease with j to enable exploration, while c_j^v increases to prevent unnecessary flight direction changes while exploring. $t_j = 1.4$ is constant. Finally, the obstacle cost is $c_j^{\text{obs}} = 1000$. This is applied in (16) so that avoiding collisions becomes the highest priority.

As with the cost parameters, the noise covariance matrix $\Sigma = \text{diag}([\sigma_{F_t} \ \sigma_{\omega_x} \ \sigma_{\omega_y}])$, which is defined in Fig. 5b, is dependent on the rollout time index j . The relative size of σ_{F_t} , σ_{ω_x} and σ_{ω_y} is based on a previous MPPI implementation [7]. The noise is reduced in the first part of the rollout to prevent noise from being applied to the UAV and also later on in the rollout where timesteps are longer to prevent erratic behaviour of the rollout trajectories. Rotation around the yaw axis is controlled separately, as described in Sec. III-C.

B. Reference Tracking

To test the ability of the GMPPI controller to follow reference trajectories, three trajectories were generated: a hover trajectory and two agile trajectories shown in Fig. 6. All trajectories specify the heading of the UAV to be equal to the projection of the velocity vectors onto the horizontal plane to allow collision avoidance using a front-mounted stereo camera.

The GMPPI controller set up with parameters from Sec. IV-A is compared to an existing standalone implementation of MPPI [7] and a standalone implementation of the SE(3) controller [8]. Three additional configurations of GMPPI are included to verify the contribution of each of the key features to the overall performance of the controller. The “no SE(3)” variant has a configuration modified with $K_{\text{SE3}} = 0$, disabling the geometric rollouts. The “const Δt ” variant includes $\mathbf{n} = [(n_{\text{exp}}) \times N]$, which equalizes the timestep lengths in all time steps of all rollouts. Finally, the “const noise” variant has all costs and noise parameters set to be constant for all time steps of all rollouts.

The results are shown in Table IV. The proposed GMPPI controller shows on average a 31% reduction in position Root Mean Square Error (RMSE) over the existing MPPI implementation [7] for agile trajectories. In the “Hover” trajectory, a 97% and 98% reduction of maximum velocity and acceleration respectively has been achieved. GMPPI exhibits a 20% higher position RMSE than the standalone SE(3) controller. This is

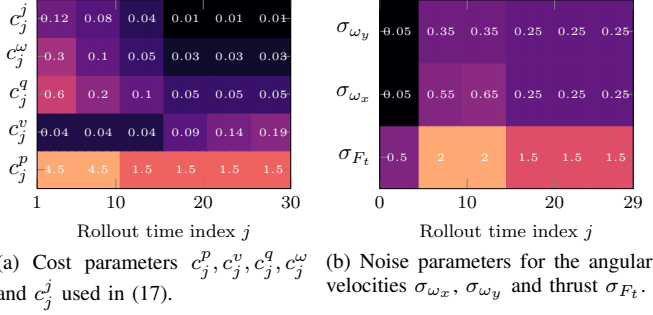


Fig. 5. GMPPI cost and noise parameters used in all experiments. A decrease in c_j^p, c_j^q and c_j^v promotes exploration. An increase in c_j^F prevents unnecessary flight direction changes. Higher noise in the middle of rollouts promotes exploration.

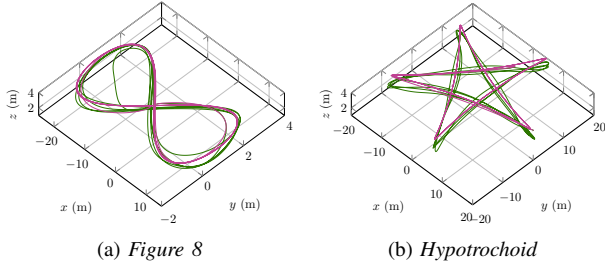


Fig. 6. Trajectories followed by GMPPI shown in green and the corresponding reference trajectories shown in red.

an effect introduced by the GMPPI cost function, which must consider all rollout trajectories, including the ones dedicated to exploring the space for obstacle-free areas. In return for this small decrease in precision, the ability to avoid obstacles on the controller level is gained, which is critical for avoiding the risk of controller short-cutting, especially in agile flights. The RMSE of heading has been reduced compared to the previous MPPI implementation [7] by an average of almost 88%. These improvements are driven by features presented in Sec. III. In particular, they highlight the synergy between SE(3) and MPPI control described in Sec. III-D. The combination of these methods yields an obstacle-aware controller retaining most of the precision of the standalone SE(3) controller.

C. Obstacle Avoidance

To verify obstacle avoidance capability, a series of flight experiments in ergodic forests [32] was carried out. Each forest contained trees of diameter 0.6m positioned according to a Poisson point process with a given density $\delta = \frac{1}{25} \text{ tree} \cdot \text{m}^{-2}$, as in [4], [9] and [5] to allow a fair comparison with the methods described therein. A straight-line reference trajectory goes 40m through the forest at a given speed ranging from 3ms^{-1} to 13ms^{-1} . A forest realization is shown in Fig. 7.

The results of the simulated experiments are shown in Fig. 8, where the ‘‘Bubble’’ results are from [9], the ‘‘Learning’’ results are from [4], and the ‘‘Dif. physics’’ results are from [5]. In the given forest density, the proposed GMPPI controller achieves a 100% success rate up to a speed of 11ms^{-1} , surpassing all learning-based methods, with failures at higher speeds occurring at challenging sections of the forest with higher local densities. At 13ms^{-1} , the proposed method has 80% less unsuccessful attempts than the Bubble planner [9].

TABLE IV
RESULTS OF REFERENCE TRACKING EXPERIMENTS.

Traj.	Controller	$\ v\ _{\max}$	$\ a\ _{\max}$	Pos. RMSE [m]	Hdg. RMSE [°]
Hover	Ours	0.01	0.08	$0.01 \pm < 0.01$	0.01 ± 0.01
	Ours(no SE(3))	0.36	1.78	0.05 ± 0.03	0.04 ± 0.05
	Ours(const Δt)	1.59	2.81	0.64 ± 0.37	0.11 ± 0.09
	Ours(const noise)	1.59	2.58	0.59 ± 0.35	0.11 ± 0.10
	MPPI	0.34	3.35	0.03 ± 0.02	6.30 ± 4.93
	SE(3)	0.01	0.02	$< 0.01 \pm < 0.01$	$< 0.01 \pm < 0.01$
Figure 8	Ours	16.93	19.12	0.85 ± 0.64	8.08 ± 8.62
	Ours(no SE(3))	15.55	18.27	1.20 ± 0.81	7.04 ± 8.06
	Ours(const Δt)	15.00	20.82	0.74 ± 0.42	6.74 ± 8.92
	Ours(const noise)	14.99	16.73	0.63 ± 0.43	7.04 ± 8.69
	MPPI	14.40	16.85	0.91 ± 0.61	31.38 ± 20.16
	SE(3)	15.02	17.27	0.52 ± 0.33	1.43 ± 1.57
Hypotrochoid	Ours	16.64	24.02	0.84 ± 0.44	11.27 ± 11.94
	Ours(no SE(3))	18.19	48.46	2.41 ± 1.69	25.92 ± 30.62
	Ours(const Δt)	15.81	29.15	0.53 ± 0.25	12.07 ± 13.03
	Ours(const noise)	18.64	46.19	0.875 ± 1.35	12.80 ± 13.38
	MPPI	18.35	22.22	1.06 ± 0.69	70.53 ± 49.51
	SE(3)	16.45	21.82	0.85 ± 0.56	1.68 ± 1.66

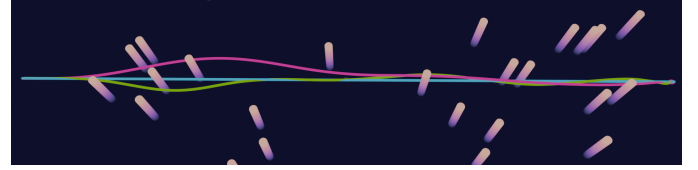


Fig. 7. Sample realization of a forest at a density $\delta = 1/25$, with the reference trajectory in blue and actual trajectories taken by the UAV when controlled by GMPPI at 5ms^{-1} and 10ms^{-1} in green and red respectively. GMPPI balances the precision and smoothness while avoiding obstacles, which leads to slightly different trajectories at different flight speeds.

It is worth noting that the Bubble planner uses a sensor with a range of 8 m, while the GMPPI controller had the rollouts length limited to 10 m.

D. Real-world experiments

Experiments with collision-free trajectories at speeds of up to 17ms^{-1} and accelerations of up to 35ms^{-2} were conducted to validate controller performance. In a figure 8-shaped trajectory with maximum speed of 14ms^{-1} and acceleration of 26ms^{-2} , GMPPI achieved a position RMSE of 0.69 m, showing no performance loss compared to simulation. To verify obstacle avoidance capability in the real world, a total of 42 flights were conducted through an obstacle course composed of seven pylons, which simulated trees, but allowed preserving

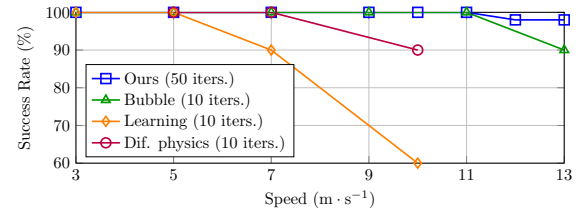


Fig. 8. Graph of success rates for different controllers in the Poisson forest in simulated experiments. Bubble results are from [9], Learning results are from [4] and Dif. physics results are from [5].

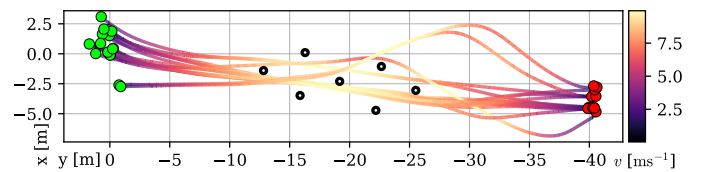


Fig. 9. Real-world flight using the GMPPI controller. Filled lines represent UAV trajectories; black dots denote obstacles, and green/red dots mark the start/end points. Obstacle density is $\delta = \frac{1}{12} \text{ pylons} \cdot \text{m}^{-2}$ with a maximum reference velocity of 10ms^{-1} .

TABLE V
MINIMUM DISTANCE TO OBSTACLES - STATISTICS

Velocity	Count	Mean [m]	Std. Deviation [m]	Worst-case [m]
10 m s^{-1}	15	0.38	0.14	0.18
7 m s^{-1}	5	0.34	0.07	0.24
3 m s^{-1}	6	0.56	0.09	0.44

localisation capability based on RTK GPS. A virtual ceiling was added to prevent the UAV from flying over the obstacles. Of the 42 conducted flights, 26 were carried out using a straight line reference trajectory through a pylon configuration shown in Fig. 1 with a density of $\delta = \frac{1}{12} \text{ pylons} \cdot \text{m}^{-2}$. These flight paths and the obstacle layout are shown in Fig. 9. The remaining experiments were carried out at speeds 3 m s^{-1} and 7 m s^{-1} . No collision has been recorded and the statistics of minimum distances to obstacles are shown in Table V.

V. CONCLUSION

We presented GMPPI, a controller for precise agile tracking with obstacle avoidance. To our knowledge, it is the first to combine sampling-based MPPI with geometric SE(3) control. The ability to track agile trajectories was tested in simulation, with speeds up to 16 m s^{-1} and acceleration in excess of 22 m s^{-2} . The results show that the controller achieves similar position RMSE to the SE(3) controller on agile trajectories. At the same time, our controller outperformed learning-based methods as well as the state-of-the-art obstacle-aware Bubble planner in obstacle avoidance capabilities. In real-world experiments, GMPPI showed no decrease in performance in following agile trajectories, and it was able to avoid obstacles at speeds of up to 10 m s^{-1} .

REFERENCES

- [1] D. C. Schedl, I. Kurmi, and O. Bimber, "An autonomous drone for search and rescue in forests using airborne optical sectioning," *Science Robotics*, vol. 6, no. 55, p. eabg1188, 2021.
- [2] A. Ollero, A. Suarez, C. Papaioannidis, I. Pitas, J. M. Marredo, V. Duong, E. Ebeid, V. Kratky, M. Saska, C. Hanoune *et al.*, "Aerial-core: Ai-powered aerial robots for inspection and maintenance of electrical power infrastructures," *arXiv preprint arXiv:2401.02343*, 2024.
- [3] P. Petracek, V. Kratky, T. Baca, M. Petrlík, and M. Saska, "New era in cultural heritage preservation: Cooperative aerial autonomy for fast digitalization of difficult-to-access interiors of historical monuments," *IEEE Robotics & Automation Magazine*, vol. 31, no. 2, pp. 8–25, 2024.
- [4] A. Loquercio, E. Kaufmann, R. Ranftl, M. Müller, V. Koltun, and D. Scaramuzza, "Learning high-speed flight in the wild," *Science Robotics*, vol. 6, no. 59, p. eabg5810, 2021.
- [5] Y. Zhang, Y. Hu, Y. Song, D. Zou, and W. Lin, "Back to newton's laws: Learning vision-based agile flight via differentiable physics," 2024.
- [6] D. Scaramuzza and E. Kaufmann, "Learning agile, vision-based drone flight: from simulation to reality," 2023.
- [7] M. Minařík, R. Pěnička, V. Vonásek, and M. Saska, "Model predictive path integral control for agile unmanned aerial vehicles," in *2024 IEEE/RSJ International Conference on Intelligent Robots and Systems (IROS)*, 2024, pp. 13 144–13 151.
- [8] T. Lee, M. Leok, and N. H. McClamroch, "Geometric tracking control of a quadrotor uav on se(3)," in *49th IEEE Conference on Decision and Control (CDC)*, 2010, pp. 5420–5425.
- [9] Y. Ren, F. Zhu, W. Liu, Z. Wang, Y. Lin, F. Gao, and F. Zhang, "Bubble planner: Planning high-speed smooth quadrotor trajectories using receding corridors," in *2022 IEEE/RSJ International Conference on Intelligent Robots and Systems (IROS)*, 2022, pp. 6332–6339.
- [10] S. Sun, A. Romero, P. Foehn, E. Kaufmann, and D. Scaramuzza, "A comparative study of nonlinear mpc and differential-flatness-based control for quadrotor agile flight," *IEEE Transactions on Robotics*, vol. 38, pp. 1–17, 12 2022.
- [11] G. Garimella, M. Sheckells, and M. Kobilarov, "Robust obstacle avoidance for aerial platforms using adaptive model predictive control," in *2017 IEEE International Conference on Robotics and Automation (ICRA)*, 2017, pp. 5876–5882.
- [12] O. Khatib, "Real-time obstacle avoidance for manipulators and mobile robots," in *IEEE International Conference on Robotics and Automation*, vol. 2, 1985, pp. 500–505.
- [13] J. Borenstein and Y. Koren, "The vector field histogram-fast obstacle avoidance for mobile robots," *IEEE Transactions on Robotics and Automation*, vol. 7, no. 3, pp. 278–288, 1991.
- [14] I. Ulrich and J. Borenstein, "Vfh+: reliable obstacle avoidance for fast mobile robots," in *Proceedings. 1998 IEEE International Conference on Robotics and Automation*, vol. 2, 1998, pp. 1572–1577 vol.2.
- [15] A. Budiyo, A. Cahyadi, T. B. Adji, and O. Wahyunggoro, "Uav obstacle avoidance using potential field under dynamic environment," in *2015 International Conference on Control, Electronics, Renewable Energy and Communications (ICCEREC)*, 2015, pp. 187–192.
- [16] F. Fraundorfer, L. Heng, D. Honegger, G. H. Lee, L. Meier, P. Tanskanen, and M. Pollefeys, "Vision-based autonomous mapping and exploration using a quadrotor mav," in *IEEE/RSJ International Conference on Intelligent Robots and Systems*, 2012, pp. 4557–4564.
- [17] B. T. Lopez and J. P. How, "Aggressive 3-d collision avoidance for high-speed navigation," in *2017 IEEE International Conference on Robotics and Automation (ICRA)*, 2017, pp. 5759–5765.
- [18] S. Liu, K. Mohta, N. Atanasov, and V. Kumar, "Search-based motion planning for aggressive flight in se(3)," *IEEE Robotics and Automation Letters*, vol. 3, no. 3, pp. 2439–2446, 2018.
- [19] J. Tordesillas, B. T. Lopez, J. Carter, J. Ware, and J. P. How, "Real-time planning with multi-fidelity models for agile flights in unknown environments," in *2019 International Conference on Robotics and Automation (ICRA)*, 2019, pp. 725–731.
- [20] K. Mohta, K. Sun, S. Liu, M. Watterson, B. Pfrommer, J. Svacha, Y. Mulgaonkar, C. J. Taylor, and V. Kumar, "Experiments in fast, autonomous, gps-denied quadrotor flight," in *2018 IEEE International Conference on Robotics and Automation (ICRA)*, 2018, pp. 7832–7839.
- [21] D. Mellinger and V. Kumar, "Minimum snap trajectory generation and control for quadrotors," in *IEEE International Conference on Robotics and Automation*, 2011, pp. 2520–2525.
- [22] Z. Wang, X. Zhou, C. Xu, and F. Gao, "Geometrically constrained trajectory optimization for multicopters," *IEEE Transactions on Robotics*, vol. 38, no. 5, pp. 3259–3278, 2022.
- [23] X. Dai, Y. Mao, T. Huang, N. Qin, D. Huang, and Y. Li, "Automatic obstacle avoidance of quadrotor uav via cnn-based learning," *Neurocomputing*, vol. 402, pp. 346–358, 2020.
- [24] J. Heeg, Y. Song, and D. Scaramuzza, "Learning quadrotor control from visual features using differentiable simulation," 2024.
- [25] M. Kazim, J. Hong, M.-G. Kim, and K.-K. K. Kim, "Recent advances in path integral control for trajectory optimization: An overview in theoretical and algorithmic perspectives," *Annual Reviews in Control*, vol. 57, p. 100931, 2024.
- [26] G. Williams, P. Drews, B. Goldfain, J. M. Rehg, and E. A. Theodorou, "Aggressive driving with model predictive path integral control," in *2016 IEEE International Conference on Robotics and Automation (ICRA)*, 2016, pp. 1433–1440.
- [27] G. Williams, B. Goldfain, P. Drews, K. Saigol, J. M. Rehg, and E. A. Theodorou, "Robust sampling based model predictive control with sparse objective information," *Robotics: Science and Systems XIV*, 2018.
- [28] Y. Li, Q. Zhu, and A. Elahi, "Quadcopter trajectory tracking based on model predictive path integral control and neural network," *Drones*, vol. 9, no. 1, 2025.
- [29] Y. Zhai, R. Reiter, and D. Scaramuzza, "Pa-mpci: Perception-aware model predictive path integral control for quadrotor navigation in unknown environments," 2025. [Online]. Available: <https://arxiv.org/abs/2509.14978>
- [30] T. Baca, M. Petrlík, M. Vrba, V. Spurný, R. Penicka, D. Hert, and M. Saska, "The MRS UAV System: Pushing the Frontiers of Reproducible Research, Real-world Deployment, and Education with Autonomous Unmanned Aerial Vehicles," *Journal of Intelligent & Robotic Systems*, vol. 102, no. 1, p. 26, May 2021.
- [31] Z. Wang, H. Ye, C. Xu, and F. Gao, "Generating large-scale trajectories efficiently using double descriptions of polynomials," in *IEEE International Conference on Robotics and Automation (ICRA)*. IEEE Press, 2021, p. 7436–7442.
- [32] S. Karaman and E. Frazzoli, "High-speed flight in an ergodic forest," in *IEEE International Conference on Robotics and Automation*, 2012, pp. 2899–2906.